Accepted Manuscript

An approach to modeling blast and fragment risks from improvised explosive devices

Matthew A. Price, Vinh-Tan Nguyen, Oubay Hassan, Ken Morgan

Please cite this article as: Matthew A. Price, Vinh-Tan Nguyen, Oubay Hassan, Ken Morgan, An approach to modeling blast and fragment risks from improvised explosive devices, *Applied Mathematical Modelling* (2017), doi: 10.1016/j.apm.2017.06.015

Highlights

- We develop a method for simulating improvised explosive detonation with fragments.

- The effect of charge shape on fragment acceleration is investigated.

- The probability of blast injuries is assessed from the simulations.

- The method is applied to model realistic scenarios involving improvised explosives.

An approach to modeling blast and fragment risks from improvised explosive devices

Matthew A. Price[a,*], Vinh-Tan Nguyen[a], Oubay Hassan[b], Ken Morgan[b]

[a]*Institute of High Performance Computing, 1 Fusionopolis Way, #16-16, Singapore 138632*
[b]*College of Engineering, Swansea University, Bay Campus, Fabian Way, Swansea SA1 8EN, UK*

Abstract

In this paper, we develop numerical methods for modeling blast and fragments generated from explosive detonation and apply them to scenarios representing improvised explosive devices in confined spaces. The detonation of condensed phase explosives is modeled with a programmed burn method in a three-dimensional multimaterial flow solver. This solver has been coupled with a Lagrangian particle solver to model the acceleration of explosive-driven fragments. We first simulate an explosion in a long cylindrical tube to validate the fluid solver for a partially-confined blast. We then simulate explosions on a subway train platform for 10 kg and 30 kg C4 charges. The maximum shock overpressure and impulse are used to predict the risk of common blast injuries. To represent improvised explosive threats, we model C4 charges with spherical, cylindrical, and disk shapes that are surrounded by a layer of spherical fragments. We find that the explosive charge shape plays an important role in the acceleration of the spherical fragments. Finally, a realistic scenario of an improvised explosive detonation near a bomb technician is investigated to assess fragment trajectory and blast loads in the near field.

Keywords: Computational fluid dynamics, Improvised explosives, Detonation, Particles, Fragments, Shock waves

*Corresponding Author.
Email address:* `mprice@lanl.gov` (Matthew A. Price)

1. Introduction

Improvised explosive devices (IEDs) represent a growing international threat, as they are often used for terrorism or sabotage. Even a small person-borne IED (PBIED) containing a few kilograms of explosive can be carried into crowded areas, or near critical infrastructures, and detonated with devastating consequence [1, 2, 3]. Modeling and simulation can provide a means to assess IED threats. Simple scenarios may be investigated with fast running engineering tools based on simplified models, but more complex cases typically require computational fluid dynamics (CFD) and multiphysics simulations. In the current work, we develop numerical simulations to investigate the detonation of small explosive charges which are representative of PBIED threats. Improvised devices are often packed with metal objects, such as nails, nuts, bolts, or ball bearings, to generate shrapnel [2]. These fragments can increase the directional force of the explosion and cause injuries at much greater distances than the blast overpressure alone [4]. Historical analysis of bombings and IED attacks have shown that secondary blast injuries, such as ballistic wounds from fragments, account for the majority of injuries observed in survivors [4, 2]. Primary blast injuries, such as eardrum rupture or pulmonary barotrauma (blast lung), are also commonly observed in bombing victims nearer to the explosion. In this work, we present a method for simulating IEDs, which can generate high velocity fragments, and assessing blast injuries. The basic underlying numerical schemes have been validated in our previous work [5, 6] and the current focus is to demonstrate their predictive capability.

There is a considerable amount of previous work for modeling explosions in urban areas. For example, Rose and Smith [7] conducted a comprehensive experimental and simulation campaign for blast propagation in various street layouts. Their tests demonstrate the "channeling" effect which enhances blast pressure and impulse when the explosion is confined by a narrow street. Advances in computing technology and numerical methods have made it possible to run very large-scale simulations of air blasts in real city geometries. Löhner

3

et al. [8] presented results of urban explosion simulations with an impressive 1.5×10^9 elements which run on 5×10^4 cores of a distributed computing system. Running simulations of this scale requires access to very large computing systems, which are not always available to the researcher. Fortunately, it is

35 possible to achieve accurate blast predictions from coarser grid simulations on workstations, or even notebook computers [9], by using a multi-mesh approach with careful attention to discretization in critical areas.

The above examples consider large explosions such as vehicle bombs in outdoor environments. However, PBIED threats are likely to be smaller charges

40 that are encountered indoors or in enclosed environments. In these cases, the confined space causes multiple internal shock reflections which lead to complex pressure wave profiles. This amplifies the lethal effect of blast waves and is associated with higher levels of injury [1, 2, 3]. The complexities of internal blast loading are discussed by Baker [10] and can be observed in various sce-

45 narios such as explosions in tunnels [11], underground train stations and train carriages [12], and buses [3]. Trains and transit stations can be high-impact targets for terrorists, as demonstrated by recent attacks in London (2005), Moscow (2004, 2010), and Madrid (2004) [13]. This provides an impetus for the tunnel and subway explosion scenarios considered in our current work.

50 Predicting the acceleration of fragments is another important aspect of IED modeling. For cased charges, a first-principles model of fragmentation would require coupling the detonation gases flow with a structural dynamics solver that has a complete material model, constitutive model, and fracturing scheme for the casing. Such methods have been applied to modeling warhead fragmen-

55 tation [14], but for the current work we seek a less computationally expensive model. Lagrangian particle methods can be used to represent fragments and readily coupled with existing compressible flow solvers. Point-particle methods are well-suited to represent small particles in flows with strong shocks [15, 16]. However, there are some notable limitations of the point-particle model when

60 applied to explosive-driven fragments [6]. The difficulty lies in representing typical fragments, which have dimensions on the order of several millimeters. In

4

conventional point-particle methods, the particle diameter (d_p) should be less than the fluid grid size (δ). We relax this requirement by assuming there are a relatively small number of particles, which generally will not occupy the same

65 fluid cell. In practice, this allows smaller grid sizes of around $\delta = 0.5d_p$. Additionally, the cell size over the explosive geometry needs to be sufficiently small for an accurate resolution of the detonation shock. Programmed burn detonation models do not resolve the reaction zone, but a pseudo-reaction zone with a length of a couple computational cells is created. Experience has shown that the

70 detonation model works well when there are at least 20 cells across the explosive thickness. Combining these constraints effectively prohibits the point-particle method from being used for very small (or thin) charges unless the fragments are also small. On the other hand, the method is suitable for charge sizes of a few kilograms with particles a few millimeters in diameter. The current work

75 investigates scenarios with IEDs in this range.

In this paper, we describe the two-way coupled Euler-Lagrange point-particle method for modeling explosive detonations and particle acceleration. This builds upon our previous work [5, 6, 17]. We present the governing equations for the fluid in Section 2.1 and particles in Section 2.2. Then, the underlying nu-

80 merical method is discussed in Section 2.3. In Section 3, we examine test cases of explosions in confined spaces. This includes blast in a semi-confined tube and an explosion on a subway train platform to demonstrate key elements of blast risk analysis with numerical models. The Euler-Lagrange particle method is then used to model fragments accelerated by three different IED charge shapes.

85 Finally, we present a case of near field explosion with blast and fragments acting on a rigid model of a bomb technician. Some conclusions and implications of this work are discussed in Section 4.

2. Numerical Methodology

2.1. Governing equations for the multimaterial fluid

The unsteady inviscid compressible multimaterial flows are governed by the Euler equations with the five-equation model proposed by Allaire, Clerc, and Kokh [18]. The governing equations can be compactly expressed as

$$\frac{\partial \mathbf{U}}{\partial t} + \nabla \cdot \mathbf{F} = \mathbf{S} \tag{1}$$

where the conserved variables vector $\mathbf{U}$, flux vector $\mathbf{F}$, and source vector $\mathbf{S}$ are defined by

$$\mathbf{U} = \begin{pmatrix} z_1 \rho_1 \\ z_2 \rho_2 \\ \rho\mathbf{u} \\ \rho E \\ z_1 \end{pmatrix}, \quad \mathbf{F} = \begin{pmatrix} z_1 \rho_1 \mathbf{u} \\ z_2 \rho_2 \mathbf{u} \\ \rho\mathbf{u} \otimes \mathbf{u} + p[I] \\ (\rho E + p)\mathbf{u} \\ z_1 \mathbf{u} \end{pmatrix}, \quad \mathbf{S} = \begin{pmatrix} 0 \\ 0 \\ -\boldsymbol{\mathcal{S}}_m \\ -\mathcal{S}_e \\ z_1 \nabla \cdot \mathbf{u} \end{pmatrix}. \tag{2}$$

Here, ρ is the mixture density, $\mathbf{u}$ is the velocity vector, E is the specific total energy, p is pressure, z is volume fraction, and $[I]$ is an identity tensor. The volume fraction of each fluid is $z_i \in [0, 1]$, such that $\sum_i z_i = 1$. For two materials, we have $z_2 = (1 - z_1)$. The five-equation model is expressed for two materials, but can be extended to more materials by including another phasic mass equation and transport equation for each additional material. The model assumes a single velocity and pressure for the materials. Total density and energy of the fluid mixture are

$$\rho = \sum_i z_i \rho_i, \tag{3}$$

$$\rho E = \rho e + \frac{1}{2}\rho\mathbf{u}^2. \tag{4}$$

where ρ_i is the phase density, e is the specific internal energy of the multimaterial mixture. The interphase coupling terms for the Lagrangian particles, $\boldsymbol{\mathcal{S}}_m$ and $\mathcal{S}_e$, are defined in Section 2.2. The particles are assumed to be solid and non-reactive, with inter-phase mass transfer (e.g. particle burning) and heat transfer neglected.

6

The five equation model is closed by a Mie-Grüneisen equation of state (EOS),

$$p(\rho, e) = \Gamma(\rho)[\rho e - \rho e_{\text{ref}}(\rho)] + p_{\text{ref}}(\rho) \qquad (5)$$

which can be inverted to obtain specific internal energy,

$$e(\rho, p) = \frac{p - p_{\text{ref}}(\rho)}{\rho \Gamma(\rho)} + e_{\text{ref}}(\rho). \qquad (6)$$

The Grüneisen parameter $\Gamma(\rho)$ and the reference states, $p_{\text{ref}}(\rho)$ and $e_{\text{ref}}(\rho)$, can be defined to reproduce different EOSs for gas, liquid, and solid materials [18, 19, 20]. Internal energy for the multimaterial mixture is calculated as

$$\rho e(\rho_i, p, z_i) = p \sum_i z_i \xi_i(\rho_i) - \sum_i z_i \xi_i(\rho_i) \beta_i(\rho_i) \qquad (7)$$

$$\beta_i(\rho_i) = p_{\text{ref}}(\rho_i) - \Gamma_i(\rho_i)\rho_i e_{\text{ref}}(\rho_i). \qquad (8)$$

In this manner, material EOS parameters are averaged through the reciprocal of the Grüneisen gamma,

$$\xi_i(\rho_i) = \frac{1}{\Gamma_i(\rho_i)}. \qquad (9)$$

95

Simulations of explosive detonation use the ideal gas EOS for the air, shock-wave EOS for the unreacted explosive, and Jones-Wilkins-Lee (JWL) EOS for the detonation products. Nonlinear EOSs, such as the shock-wave and JWL EOS, are necessary for modeling materials under very high pressures. Parameters for the JWL EOS are ω, A, B, R_1, R_2, and initial density ρ_0. JWL parameter sets for many explosives can be found in the literature [21]. A generic set of shock wave EOS parameters for the unreacted explosive are automatically calculated by the programmed burn model [5].

The programmed burn model handles the conversion of the unreacted solid explosive to reacted detonation products. It requires input of the detonation pressure p_{CJ}, detonation velocity D_{CJ}, and detonation energy e_{det}. Ignition time for explosive cells is calculated as the time taken for the detonation wave to travel from the initiation point to the explosive cell center. Explosive burning is tracked by a reaction variable, $\lambda \in [0, 1]$, which is incremented as the cell

7

burns. EOS for the burning explosive is treated as a submodel in the multimaterial framework with internal energy and pressure calculated using λ-averaged values of the EOS functions $\xi_i(\rho_i)$ and $\beta_i(\rho_i)$. The initial internal energy of the unreacted explosive includes e_{det}, so that the products gain the detonation energy after the reaction is complete. More details on this methodology can be found in [5]. In practice, this provides an inexpensive method for handling an additional EOS without adding to the system of governing equations. However, this method requires the explosive to be stationary during the simulation as λ is not an advected quantity.

2.2. Governing equations for particles

From Newton's law, the equations of motion for a particle are

$$\frac{d\mathbf{x}_p}{dt} = \mathbf{u}_p \tag{10}$$

$$m_p \frac{d\mathbf{u}_p}{dt} = \mathbf{F}_{\text{qs}} + \mathbf{F}_{\text{pg}} + \mathbf{F}_{\text{am}} \tag{11}$$

where m_p is the mass, $\mathbf{x}_p$ is position, and $\mathbf{u}_p$ is velocity of the particle. Particle forces include the quasi-steady drag $\mathbf{F}_{\text{qs}}$, the pressure-gradient $\mathbf{F}_{\text{pg}}$, and the added-mass $\mathbf{F}_{\text{am}}$ forces. Particle heating under unsteady shock interactions is included in some particle models in the literature [22, 15, 16], but typically for small lightweight particles. For particles much larger that the reaction zone, Ripley et al. [22] found that particle heating is mainly due to shock compression and a non-heat-conducting assumption is valid. Therefore, heat transfer terms are neglected for the large rigid particles assumed here. We neglect other forces, such as body forces (buoyancy, gravity, electromagnetic, etc.), lift, and viscous unsteady history forces. Particle-particle interactions are unlikely in the current models and are also neglected. The forces on a spherical particle are

$$\mathbf{F}_{\text{qs}} = \frac{\pi d_p^2}{8} \rho_{\text{f,p}} C_D |\mathbf{u}_{\text{f,p}} - \mathbf{u}_p| (\mathbf{u}_{\text{f,p}} - \mathbf{u}_p) \tag{12}$$

$$\mathbf{F}_{\text{pg}} = -V_p \left(\nabla p_{\text{f,p}} \right) \tag{13}$$

$$\mathbf{F}_{\text{am}} = -C_M V_p \left[\nabla p_{\text{f,p}} + \frac{d \left(\rho_{\text{f,p}} \mathbf{u}_p \right)}{dt} \right] \tag{14}$$

8

where V_p is the particle volume, and $\rho_{\mathrm{f,p}}$ and $\mathbf{u}_{\mathrm{f,p}}$ are the fluid density and velocity at the particle location, respectively. The Eulerian fluid variables at the Lagrangian particle locations (subscript 'f,p') are evaluated by a linear interpolation from neighboring fluid grid points. The drag coefficient C_D for spherical particles is found from empirical correlations as a function of the particle Reynolds number (Re_p) and Mach number (M_p),

$$Re_p = \frac{\rho_{\mathrm{f,p}}\, d_p}{\mu_{\mathrm{f}}}|\mathbf{u}_{\mathrm{f,p}} - \mathbf{u}_p|, \tag{15}$$

$$M_p = |\mathbf{u}_{\mathrm{f,p}} - \mathbf{u}_p|/c_{\mathrm{f,p}}. \tag{16}$$

Here, c_{f} is the fluid sound speed and μ_{f} is dynamic viscosity of the fluid from Sutherland's law. Based on our previous studies [6], we have chosen the drag correlation of Loth [23] because it includes the effects of fluid compressibility at higher Mach numbers ($M_p > 0.3$) and also provides valid C_D values at high Reynolds numbers ($Re_p > 10^5$) which occur during explosions. For the added mass coefficient, C_{M}, we adopt an expression which is a function of M_p to account for the effects of fluid compressibility [24]. C_{M} has values between 0.5 and 1.0 [6].

The interphase coupling terms for particle momentum $\boldsymbol{\mathcal{S}}_m$ and work transfer $\mathcal{S}_e$ are calculated for each fluid cell as

$$\boldsymbol{\mathcal{S}}_m(\mathbf{x}_c) = \frac{1}{V_f} \sum_{i=1}^{N} \mathcal{G}_i\left(\mathbf{x}_c, \mathbf{x}_p^i\right) \left(\mathbf{F}_{\mathrm{qs}}^i + \mathbf{F}_{\mathrm{pg}}^i + \mathbf{F}_{\mathrm{am}}^i\right), \tag{17}$$

$$\boldsymbol{\mathcal{S}}_e(\mathbf{x}_c) = \frac{1}{V_f} \sum_{i=1}^{N} \mathcal{G}_i\left(\mathbf{x}_c, \mathbf{x}_p^i\right) \left(\mathbf{F}_{\mathrm{qs}}^i + \mathbf{F}_{\mathrm{pg}}^i + \mathbf{F}_{\mathrm{am}}^i\right) \mathbf{u}_p^i. \tag{18}$$

The interpolation function $\mathcal{G}_i$ is used to transfer particle forces from the set of particles N with coordinates $\mathbf{x}_p^i$ to the associated fluid cell having coordinates $\mathbf{x}_c$. The total particle force is averaged by the volume of the fluid cell, V_f. The acceleration of large particles from rest can cause a flow reversal, or possibly even negative pressures, due to the excessive extraction of fluid momentum. This is more likely to occur when particles are large ($d_p > \delta$) or closely spaced. To prevent large forces concentrated at single fluid grid points, the forces are

9

135 spread over a larger region of surrounding fluid cells [6]. For extreme cases, limiters may also be applied to the interphase source terms.

2.3. Spatial and temporal discretization

The Euler equations for fluid flow are solved with a vertex-centered, edge-based finite volume method on unstructured grids. The three-dimensional com-
140 putational domain is discretized into non-overlapping tetrahedral elements using a robust Delaunay mesh generation method [25]. A median dual mesh is constructed by connecting edge midpoints, element centroids, and face centroids such that only one node is present in each control volume. The HLLC approximate Riemann solver [26] is used for calculation of the inviscid flux of conser-
145 vative variables and the advection equation. Second-order accuracy is achieved by solving the local Riemann problem with reconstructed values at the left and right states [17]. Gradients are computed from a Green-Gauss method using the primitive variables ($\rho_1 z_1$, $\rho_2 z_2$, u, v, w, P, z), to avoid pressure oscillations at the interface [18]. The Barth-Jespersen limiter is used to control instabilities
150 near steep gradients after reconstruction [27].

Time discretization of the governing fluid equation utilizes a minimal storage Runge-Kutta formulation [28] which requires only one extra copy of the right hand side terms and unknowns be stored. The time step (Δt) is calculated through the Courant-Friedrichs-Lewy condition. For a second-order accurate
155 solution, the two-stage scheme has coefficients $\alpha_1 = 0.5$ and $\alpha_2 = 1.0$. The system of nonlinear ordinary differential equations for the particles is solved sequentially with the fluid equations using the same time step and temporal discretization method.

2.4. 1D multimaterial solver

160 A one dimensional Eulerian multimaterial solver, "1DMM", has been developed which employs the same methodology as the 3D compressible fluid solver described above. Specifically, it solves the five-equation multimaterial model using an HLLC approximate Riemann solver and the programmed burn

10

detonation model. The 1D solver is able to represent planar, cylindrical, and
spherical symmetry conditions through the use of geometric source terms. With
the 1DMM solver, we are able to study one dimensional problems with much
finer grid resolutions than is feasible for 3D models. 1DMM solutions can also
be used to initialize 3D explosion and air blast models, for a combined 1D-3D
approach.

2.5. Blast risk evaluation

During an explosion, the rapid expansion of detonation gases compresses
the surrounding air and creates a shock wave. The air is initially at an ambient
pressure, p_0, but jumps to the peak overpressure, p_m, at the shock arrival time,
t_a. The pressure then rapidly decays until it reaches p_0, marking the end of
the positive phase. This is usually followed by a negative phase, when the
overpressure temporarily drops below the ambient pressure, due to the over-
expansion of the high velocity detonation products. Gas-filled organs of the
body, such as the ears, lungs, sinuses, and bowels, are susceptible to rupture
from both positive and negative pressure waves. The effect of explosions on the
brain, i.e. traumatic brain injuries, are now more widely recognized [4]. While
some thresholds for brain injuries have been suggested, they are not assessed
in the current work as there are multiple injury mechanisms and they remain
difficult to predict and diagnose [29].

Blast severity is commonly characterized by values of peak overpressure and
maximum positive phase impulse, I_m. Negative phase pressure and impulse
are generally neglected in risk analysis because they are much lower and less
likely to cause injury [4]. For explosions in confined spaces, multiple secondary
shocks can contribute to the positive phase impulse. The peak overpressure and
maximum impulse in the simulations are evaluated as

$$p_\mathrm{m} = \max\left(p(t) - p_0\right) \quad \forall\, t \in [0, t_\mathrm{sim}], \tag{19}$$

$$I_\mathrm{m} = \max\left(\int_0^t [p(t) - p_0]\, dt\right) \quad \forall\, t \in [0, t_\mathrm{sim}], \tag{20}$$

on all wall surfaces over the entire simulated time, t_sim.

11

Comprehensive reviews of models predicting injury from explosions are given by Baker [10] and Lees [30]. Probit equations, which relate the statistical probability unit (Y) to injury factors, are widely used to assess hazards in the process industries and are also straightforward to apply during post-processing of the numerical results. First we consider primary blast injuries, which result from direct interaction of the high pressure waves. These include tympanic membrane (eardrum) rupture and lung hemorrhage. Eardrum injuries have lowest threshold (i.e. greatest chance of occurring), but are nonfatal. The probit equation for eardrum rupture,

$$Y_{\mathrm{E}} = -12.6 + 1.524 \ln(p_{\mathrm{m}}) \tag{21}$$

is solely a function of p_{m} (Pa) [30]. The mechanisms of blast induced lung injuries are complex and remain a topic of considerable research [31, 29]. Bowen et al. [32] analyzed a large collection of experimental data on thirteen mammalian species and developed 24-hour survival curves for a 70 kg man at different orientations with respect to the blast wave. While the Bowen curves are usually plotted against pressure and positive phase duration, they can also been presented as pressure-impulse (PI) graphs [10]. Probit equations developed from PI graphs in the TNO Green Book [33] can be simplified to

$$Y_{\mathrm{L}} = 5 - 5.74 \ln \left(\frac{4.26 \times 10^5}{p_{\mathrm{eff}}} + \frac{1705}{I_{\mathrm{m}}} \right) \tag{22}$$

where I_{m} has units (Pa-s). The effective peak overpressure, p_{eff} (Pa), can vary depending on the orientation of the person to the blast and nearby surfaces. To represent the worst-case, p_{eff} is assumed to be the peak reflected overpressure [30], and calculated as

$$p_{\mathrm{eff}} = p_r = 2 p_{\mathrm{m}} \left(\frac{7 p_0 + 4 p_{\mathrm{m}}}{7 p_0 + p_{\mathrm{m}}} \right). \tag{23}$$

Although the Bowen curves are considered a standard in evaluating lung injury, they were developed from free-field blasts and have questionable applicability for more complex blast scenarios. Consequently, several improved or alternative models have been developed [4, 29, 34]. Bass et al. [35] analyzed a

12

large set of animal experiments for short duration blasts (< 30 ms) and proposed somewhat improved curves. Axelsson and Yelverton [36] developed a mathematical model linking chest wall velocity to injuries and validated it with blast testing on sheep in various enclosed areas. The level of trauma to the lungs, upper respiratory tract, gastrointestinal tract and solid intra-abdominal organs was quantified by the adjusted severity of injury index (ASII). van Doormaal et al. [37] proposed a simplified single point approach to the Axelsson model. In their approximate approach, the inward chest wall velocity V_{Ax} (m/s) due to a shock load with a single peak is

$$\frac{V_{\mathrm{Ax}}}{p_{\mathrm{m}}} = \begin{cases} -4.1863\,t_{\mathrm{eq}}^2 + 2.003{\times}10^{-2}\,t_{\mathrm{eq}} + 7.982{\times}10^{-9}, & \text{if } t_{\mathrm{eq}} \leq 0.001 \text{ s} \\ f_1(p_{\mathrm{m}}, I_{\mathrm{m}})\,f_2(p_{\mathrm{m}}) + 1.589{\times}10^{-5}, & \text{otherwise} \end{cases} \tag{24}$$

where $t_{\mathrm{eq}} = \frac{2\,I_{\mathrm{m}}}{p_{\mathrm{m}}}$ is the equivalent triangular pulse duration and

$$f_1(p_{\mathrm{m}}, I_{\mathrm{m}}) = \frac{4.5{\times}10^{-5}}{1 + \exp\left[\frac{-6.806 - \ln(t_{\mathrm{eq}})}{0.845}\right]} - 2.1147{\times}10^{-5}, \tag{25}$$

$$f_2(p_{\mathrm{m}}) = -7.3786{\times}10^{-19}p_{\mathrm{m}}^3 + 1.8576{\times}10^{-12}p_{\mathrm{m}}^2 - 2.0727{\times}10^{-6}p_{\mathrm{m}} + 1.579. \tag{26}$$

The correlation between ASII and chest wall velocity determined from the experiments and models is

$$\mathrm{ASII} = \left(0.124 + 0.117 V_{\mathrm{Ax}}\right)^{2.63} \tag{27}$$

The ASII value can be associated with varying levels of injury. In this study, we consider only a lethality of $\geq 50\%$, which corresponds to ASII ≥ 3.6. The Axelsson model can assess injury from multiple shocks in enclosed environments. However, the procedure for approximating injury from a shock with two peaks using the single-point approach is significantly more complex [37]. This would require tracking peak pressures and impulse of individual shocks, which is not practical in large simulations. Instead, a single t_{eq} for the entire blast event is calculated directly from p_{m} and I_{m}.

Other fatal injury modes include whole body displacement with either whole body impact or head impact (skull fracture). These are evaluated from the

13

probit equations in Lees [30]:

$$Y_{\text{head}} = 5 - 8.49 \ln \left(\frac{2430}{p_{\text{m}}} + \frac{4 \times 10^8}{p_{\text{m}} \, I_{\text{m}}} \right) \tag{28}$$

$$Y_{\text{body}} = 5 - 2.44 \ln \left(\frac{7380}{p_{\text{m}}} + \frac{1.3 \times 10^9}{p_{\text{m}} \, I_{\text{m}}} \right) \tag{29}$$

Probit values are transformed to a probability of occurrence (percentage of the affected population), R, through the correlation

$$R(\%) = -3.25 Y^3 + 48.76 Y^2 - 206.60 Y + 270.35 \tag{30}$$

which is valid over the range $3.36 < Y < 6.64$ (i.e. $5\% < R < 95\%$) [38].

₁₉₅ A review of fragment injuries and models is provided by Baker [10] and Lees [30]. Incapacitating injury from fragment penetration are classified as perforation of the skull, trunk, penetration to half-depth, or penetration hitting central supporting bones of the limbs. Experiments show that the impact of fragments traveling at more than a couple hundred meters per second are gen-₂₀₀ erally associated with fatal or incapacitating injuries [30]. As IED fragment velocities are expected to be much higher than this threshold, they are assumed to be nearly always fatal and probabilities of fragment injuries are not assessed in the current work.

While experiments are limited to recording pressures at a few specific loca-₂₀₅ tions, simulations can store pertinent blast data at every grid point within the computational domain. Key blast and fragment loading criteria can then be determined through post-processing (e.g. via probit equations). However, one should exercise caution when interpreting results from probit equations as they have validity ranges corresponding to the experimental data. For example, pro-₂₁₀ bit equations for death by body displacement (skull and whole body) are limited to $p_{\text{m}} < 400$ kPa [30]. For simulation-based risk predictions, the accuracy of the numerical models should also be considered. The resolution of peak pressures and impulse are directly related to the grid spacing and particular numerical method. As an example, if p_{m} is under-predicted by 10% then the probability ₂₁₅ of eardrum rupture would only be $2 - 6\%$ lower, but if p_{m} is under-predicted by 30% then the probability of eardrum rupture is $10 - 20\%$ lower.

14

3. Results and discussion

Several IED scenarios are presented to demonstrate the methodology for simulating bare charge explosions in confined spaces, and explosives with frag-

₂₂₀ ments. Validation of the multimaterial solver and the Euler-Lagrange particle method are described in earlier works [5, 6]. In the first scenario, experimental data from an explosion in a semi-confined tube (i.e. tunnel-like geometry) provides additional validation of the flow solver. Next, an explosion on a subway platform is simulated and the potential for human injuries is assessed. In the

₂₂₅ third example, IEDs with fragments are modeled to understand the effect of charge shape on fragment acceleration. Finally, we present a case representing the detonation of an IED with fragments very near a bomb disposal technician.

A multi-step approach is used to reduce computational cost for the larger simulation cases. This technique is common in blast simulations [9, 39], because

₂₃₀ a large portion of the computational domain further away from the explosion is quiescent in early simulation times. Simulations were run on an HP Z800 workstation which has 12 processors (Intel Xeon X5650 @2.67GHz) and 32 Gb RAM. For blast simulations in the multimaterial solver, the 3D domains are first filled with the ambient air using an ideal gas EOS with $\gamma = 1.4$, $\rho_0 = 1.2$ kg/m^3,

₂₃₅ and $p_0 = 101325$ Pa. The explosive material is then patched into the domain to initialize cells in the appropriate region. The JWL EOS and detonation parameters for explosives used in this work are given in Table 1. Parameters are taken from Dobratz [21] for TNT and C4, and from Zakrisson [40] for the Swedish m/46 explosive.

₂₄₀ 3.1. Semi-confined explosion in a tube

Studies of explosions in tubes are useful in understanding the risks of IED attacks in tunnels. For example, Pennetier, William-Louis, and Langlet [11] conducted scaled tests of propane-oxygen explosions in square tubes designed to represent railway tunnels and a subway station. At full scale, their tests

₂₄₅ represented TNT charges of $0.5 - 20$ kg with a tunnel cross-section of 5×5 m.

15

Table 1: JWL EOS and detonation parameters for the explosive materials.

Explosive	ρ_0 (kg/m^3)	ω	A (GPa)	B (GPa)	R_1	R_2	D_{CJ} (m/s)	p_{CJ} (GPa)	e_{det} (MJ/kg)
TNT	1630	0.30	371.2	3.231	4.15	0.95	6930	21.0	4.294
m/46	1500	0.29	759.9	12.56	5.10	1.50	7680	21.25	4.700
C4	1601	0.25	609.8	12.95	4.50	1.40	8193	28.0	5.621

The current test is based on experiments of a detonation inside a long cylindrical steel tube, as described in [41] and illustrated in Figure 1. The tube has a diameter of 1.5 m and length of 24 m. One end is closed while the other is open to the outside environment. A 0.5 kg spherical charge of PETN-based Swedish plastic explosive (m/46) was detonated in the center of the tube at 1.0 m from the open end. It is worth noting that when scaled up by a factor of four, this test represents a 32 kg charge of m/46 in a 6 m diameter cylinder (i.e. approximate dimensions of an underground train tunnel). The external volume surrounding the open end of the cylinder is included in the model to allow for expansion of the detonation products outside of the tube. The 3D simulation is split into two steps. The first step includes a section of the tube which extends up to nine meters from the open end of the tube. Pressure measurements from two identical experiments were recorded on the cylinder wall at 12 m and 21 m from the open end of the tube.
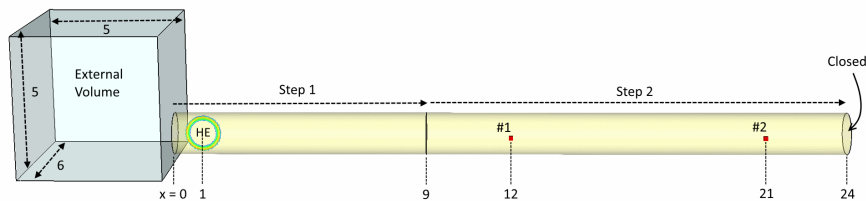

Figure 1: Schematic of the tube explosion model showing locations of the gauges and explosive (dimensions in meters). Distances from the open end of the tube ($x = 0$) are noted.

16

₂₆₀ The m/46 charge is modeled with the programmed burn model and JWL EOS parameters in Table 1. The 1DMM solver is used to provide an initial solution of the detonation which is interpolated into the step 1 domain. The 1D simulation was finely resolved, with a cell size of 1.0 mm, and were run until the shock was nearly 0.75 m from the origin ($t = 0.30$ μs). In steps 1 and 2, a

₂₆₅ constant cell size of 0.03 m is prescribed up to 0.75 m from the explosive origin. The cell size increases up to 0.05 m along the tube, and gradually increases up to a maximum of 0.15 m outside of the tube. These cell sizes were determined from mesh studies and previous work [41] to provide a good resolution of the propagating shocks. After 10 ms, the step 1 solutions are interpolated into the

₂₇₀ full domain of step 2 and the simulation continued until a final time of 120 ms. Figure 2 shows pressure contours on a cut plane at the end of step 1.
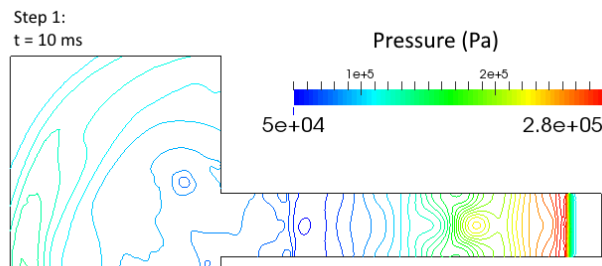

Figure 2: Pressures at $t = 10$ ms on a slice of the step 1 domain in the tube explosion.

Overpressures from the simulations are compared with test data for the two gauge locations in Figure 3. The experimental data has been processed with a low-pass filter to reduce noise. After detonation, there are multiple shock

₂₇₅ reflections from the tube walls. These shocks coalesce as they propagate down the tube forming a single shock wave that is essentially one-dimensional by the time it reaches gauges #1 and #2. Streak diagrams, shown in Figure 4, were created from the simulation using a line that runs along the tube axis through the entire domain. These can be correlated with the gauge locations
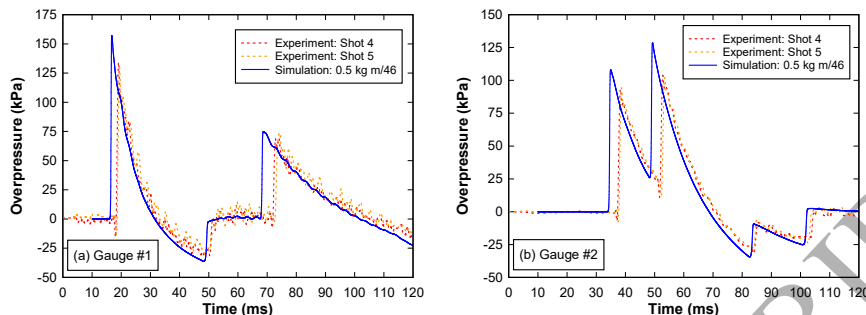
17

Figure 3: Pressure histories from the simulation and experiment at (a) 12 m and (b) 21 m from the tube opening.

for insight into the shock dynamics. Near the explosion there is a strong shock
that propagates down the tube, and rarefaction waves from the tube opening
which cause the pressure to drop significantly below the ambient value. This
occurs because the explosive detonation products expand into the large external
volume of air outside the tube, creating a very low pressure region inside the
tube. When the shock reaches the closed end of the tube, there is a strong
reflected shock which then interacts with the rarefaction wave. This reflected
shock causes the large secondary pressure peak observed (at $t \approx 70$ ms for
gauge #1 and at $t \approx 50$ ms for gauge #2). The jump in pressure for gauge #1
at $t \approx 50$ ms is due to the rarefaction wave from the open end. The other peaks
at gauge #2 ($t \approx 80$ and 100 ms) are due to the interaction of the rarefaction
wave and the reflected shock.

With the current set of JWL parameters for m/46, the simulations have
slightly earlier arrival times and higher peak pressures than the experiments.
This is possibly due to a difference in the chemical energy between the actual
explosive and JWL, or because the spherical explosive in the experiments was
hand-packed and at a lower density than the JWL parameters. Nonetheless,
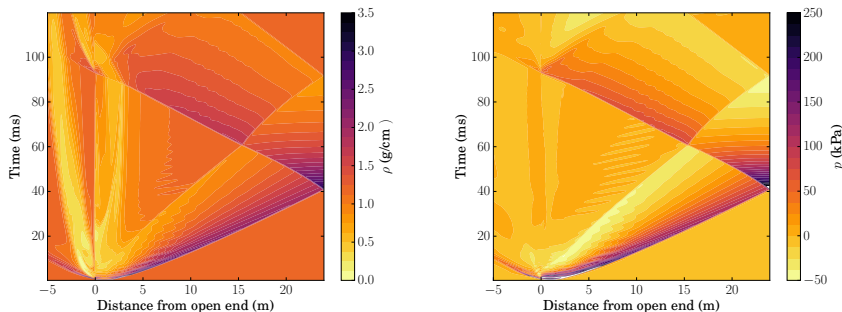the overall agreement with the test data is very good.

18

Figure 4: Streak diagrams of (a) density and (b) pressure for a line along the tube axis.

3.2. Explosion on a subway train platform

This numerical test demonstrates application of the simulation method for
risk assessment of explosions and terrorist attacks on land mass transport infras-
tructures. We investigate explosions on an underground train platform, which
is similar to previously studied cases in the literature [12, 13]. Explosive charges
of 10 kg and 30 kg C4 were chosen to represent backpack or briefcase bombs
(common PBIED threats). A short section of the train platform is modeled, as
shown in Figure 5. The tunnel section is 28.5 m long with a diameter of 6 m.
There are two entrances to the platform and three benches along the wall. A
hemispherical explosive charge is located on top of the middle bench.

Gauge points are located near the entrances to the platform and in front of
each bench. They are at 1 m height above the platform and 1 m in front of
the benches (roughly centered along the platform width). The simulation has
two steps. Step 1 has a reduced domain size of approximately $3\times4\times4.5$ m to
allow a finer mesh for the detonation calculation. The cell size is 8 mm near the
explosive and increases to a background size of 80 mm. Step 2 has a cell size
of 30 mm near the explosive which increases to a background size of 100 mm.
At the end of step 2 ($t = 100$ ms), the reflected shock pressures are reduced to
near ambient conditions and the maximum impulse has been captured. Table 5
gives a summary of mesh and run times on the HP Z800 workstation. The total
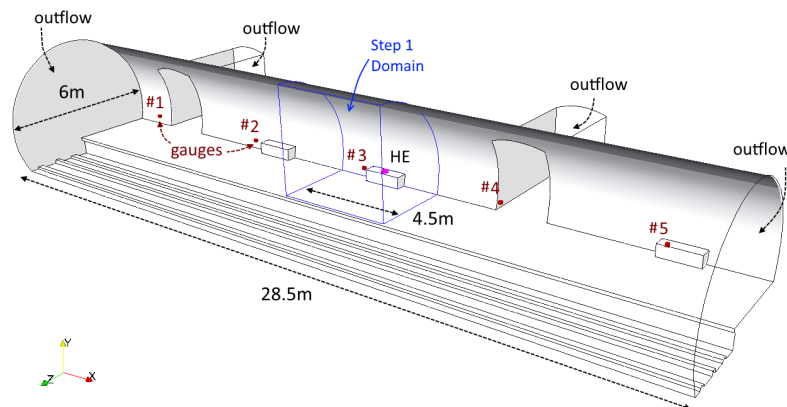number of elements (n_{el}), number of processors used (n_{CPU}), simulation time

19

Figure 5: Computational domain, IED location, and gauge locations for the subway platform explosion models.

(t_sim), and actual run time (t_solve) are given for the 10 kg C4 simulations. The
320 30 kg C4 simulations were run on the same grids, but step 1 run time and total
solve times differ slightly.

Table 2: Simulation details for the 10 kg C4 subway explosion.

Step#	n_el	n_CPU	t_sim (ms)	t_solve (hr)
1	4.35×10^6	10	$0-0.6$	2.2
2	4.23×10^6	10	$0.6-4$	~24

Pressure and impulse histories from gauges in the 10 kg C4 simulation are
plotted in Figure 6. Gauges #2 and #4 are approximately 6 m from the charge
and have nearly identical blast wave profiles. Likewise, pressures at gauges
325 #1 and #5 are similar. Gauge #3 has not been included in this comparison
because it has much higher pressures due to its proximity to the explosion.
There are many secondary shocks which contribute to the impulse. One of the
challenges for assessing internal blast loads is determining how many of the
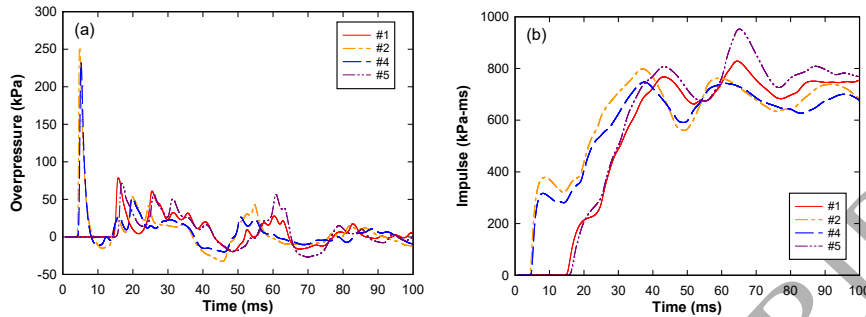secondary shocks to include in the impulse calculations (i.e. how long to run

20

Figure 6: Pressure (a) and impulse (b) histories at gauges in the subway explosion with 10 kg of C4.

330 the simulation).

The probability of eardrum rupture in the 10 kg subway explosion is shown in Figure 7. There are four regions of probability ranges indicated. The region of > 90% risk of eardrum rupture charge covers the area up to roughly 6.5 m from the explosive. Further from the explosive, the risk drops rapidly to below

335 50% but remains above 5% throughout the rest of the domain. In this scenario, shock reflections from the wall behind the charge will also cause higher pressures and injury risks on the opposite side of the tunnel (near the train tracks). Peak overpressures from an unconfined explosion have been calculated using the empirical correlations of Kingery and Bulmash [42] for a hemispherical TNT

340 surface burst (assuming a TNT equivalency of 1.37 for C4 [42]). Empirical methods are often used to predict pressure and impulse, but they do not include confinement effects. This comparison demonstrates how reflected shocks in the enclosed tunnel increase the risk of eardrum injury. Empirical blast calculations also cannot account for the shock diffraction around corners, which results in

345 lower pressures at the entrances observed in the simulations.

Figure 8 shows the regions of 50% lethality from lung injury evaluated using the Bowen curve based probit equation (Eq. 22) and the ASII criteria from the Axelsson model. Disagreement between Bowen curves and the Axelsson model has been reported in the literature [31, 34], but typically the Bowen curves
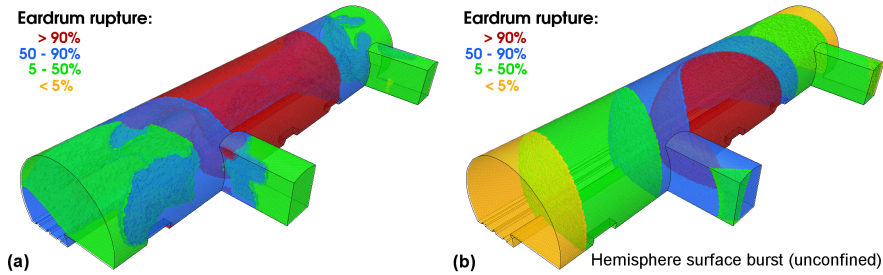
21

Figure 7: Probability of eardrum rupture on the subway platform from (a) the 10 kg C4 charge simulation and (b) an empirical-based calculation of a 13.7 kg TNT hemispherical blast.

₃₅₀ give a higher injury prediction for a given pressure and duration. However, $R(Y_{\mathrm{L}}) > 50\%$ for the 10 kg charge covers only a small area near the charge and is much lower than the Axelsson model. The reason for this can be understood through inspection of the PI graph for the Bowen curves [10, 30]. For a particular injury level, there is a minimum value of impulse that must be exceeded. For a ₃₅₅ 50% lung injury, this impulse is roughly 1705 Pa-ms, which occurs only in a few small areas of the 10 kg simulation. Interestingly, the predicted 50% lethality regions are roughly the same for the 30 kg charge. Teland et al. [34] note some shortcomings in the method used to derive the Bowen curves. For example, the blast wave duration was calculated and not measured from experiments. They ₃₆₀ found that the Axelsson model agrees with the Bowen curves for large charges and is better for complex blast scenarios. While it is tempting to favor the Axelsson model for lung injury predictions, the assumptions of the model should be kept in mind. In particular, the current analysis assumes a single pressure wave with duration estimated from an equivalent triangular pulse. With the ₃₆₅ 30 kg charge, the region of 50% risk probability extends further along the tracks than it does along the platform. This is due to the higher impulse along the tracks as the blast wave is reflected off the opposite side of the tunnel and is channeled along the tracks.

Regions of 50% probability of death from whole body displacement with ₃₇₀ body impact or head impact are shown in Figure 9. While the risk of death
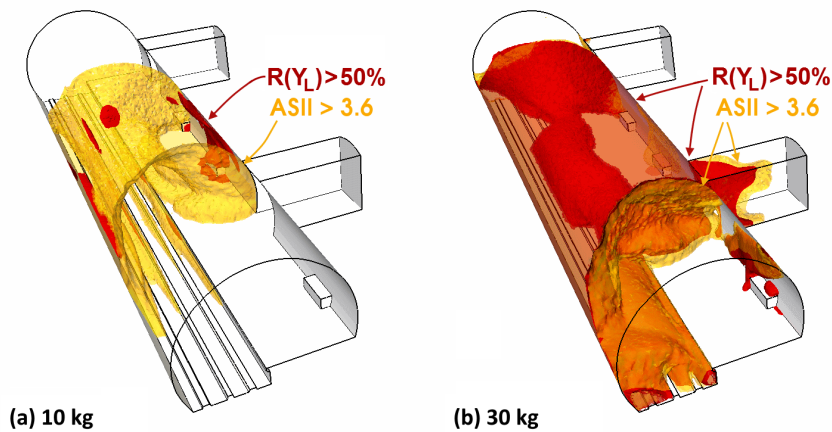
22

Figure 8: Probability of death due to lung hemorrhage during an explosion of (a) 10 kg and (b) 30 kg C4 on the subway platform. 50% risk probability regions evaluated using the Bowen curves $R(Y_\text{L})$ and chest wall velocity (ASII) methods.

from this type of injury covers a larger region than the lung injury, it is not a direct blast injury. Rather, it requires that the person be thrown by the blast into a hard surface. The risk of impact resulting in head injury (skull fracture) is higher than the body injury. For the 10 kg charge, the 50% skull fracture

375 injury risk covers an area up to roughly 5 m from the explosive. Beyond this, the probability drops very rapidly to $< 5\%$. The 30 kg charge size results in a much larger area for risk of death from whole body displacement injuries. The current simulations do not account for people or obstructions on the subway platform which would alter the blast propagation and injury risks. If the explosion were

380 to occur when a train was present at the station, then the reduction in enclosed volume is expected to amplify the blast and increase the injury risks. The presence of people or movable objects in the model would potentially decrease the size of the injury regions as some of the blast energy would be absorbed [13].

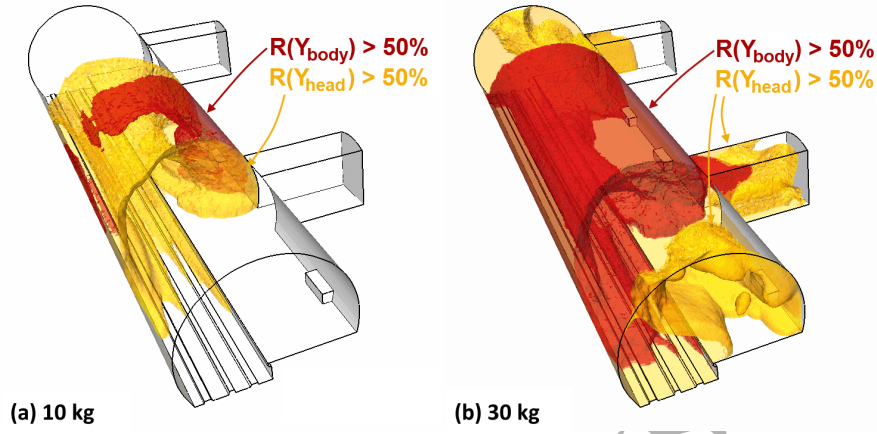385 *3.3. Explosive geometry influence on fragment acceleration*

23

Figure 9: The 50% probability of death due to whole body displacement with body impact or head impact during an explosion of (a) 10 kg and (b) 30 kg C4 on the subway platform.

Many factors can influence the acceleration of fragments during an IED detonation. These include the mass and distribution of fragments, properties of the metal, mass and energy output of the explosive, and the explosive configuration. The Gurney model is commonly used to predict velocities of fragments in contact with an explosive, such as from cased charges [42, 43]. For common symmetric configurations, the Gurney equations can be generalized as

$$V_{\mathrm{G}} = \sqrt{2E}\left[\frac{C/M}{\Phi}\right]^{1/2}, \text{where} \quad \Phi = \begin{cases} \left(1 + \frac{3}{5}\frac{C}{M}\right) & \text{for a sphere} \\ \left(1 + \frac{C}{2M}\right)\left(1 + \frac{D}{2L}\right) & \text{for a cylinder} \\ \left(1 + \frac{C}{3M}\right)\left(1 + \frac{2L}{D}\right) & \text{for a disk} \end{cases}$$
(31)

where $\sqrt{2E}$ is the Gurney characteristic velocity, which is related to the chemical energy of the explosive, and C/M is the ratio of charge mass to metal mass. These expressions account for energy losses due to finite sized charges [43]. As $L \to \infty$ for a cylinder, the equation reduces to an infinite-length cylinder configuration. Likewise, as $D \to \infty$ for a disk, the equation reduces to the symmetric sandwich configuration. For a given C/M, Gurney analysis predicts that a symmetric sandwich will produce the highest fragment velocities, followed by an infinite-length cylinder, and finally a spherical charge. This can be attributed

24

to the confinement of the detonation gases provided by each configuration.

The Gurney model assumes that most of the detonation energy is transferred into kinetic energy of the metal casing before it fractures. As the casing breaks apart, there is gas leakage and the energy transfer is terminated. Gurney characteristic velocities are based on carefully controlled experiments, and are known to overpredict velocities if fracturing occurs early [42]. Consequently, the Gurney equations are not well-suited for predicting the velocities of preformed fragments with gaps. This situation arises with IEDs which contain preformed fragments, such as nuts, bolts, nails, or ball bearings packed around an explosive. Preformed fragments have also been used in experiments, such as the dense fragment generator described by Lixin et al. [44] which used a tamped conical/disk-shaped charge to drive 5 mm steel balls. In their Gurney analysis, Lixin et al. applied a 'correction factor' which reduced the predicted V_G by 10%.

The objective of the current numerical study was to investigate IED fragment acceleration for different charge geometries. The 3D simulations consist of symmetric configurations of spherical, cylindrical, and disk shaped C4 explosive charges surrounded by a layer of spherical fragments. The simulations utilized three symmetry planes to reduce computational cost. Simulation domains with dimensions are shown in Figure 10 for the different configurations. The fragments were modeled as Lagrangian particles which were located around the radius of the sphere and cylinders, and on the ends of the disks. In each case, the effective charge thickness (the distance from the center of the explosive to the nearest surface) was 50 mm. However, this constraint results in a varying charge mass for the different explosive geometries. Computational domain sizes were large enough to allow the particles to reach a constant terminal velocity,

$$V_T^i \equiv \max | \, \mathbf{u}_p^i(t) \, |, \quad \forall \, t \in [0, t_{\text{sim}}]. \tag{32}$$

The study included two length-to-diameter (L/D) ratios for cylindrical and disk charges to assess the effect of increased geometric confinement (reduced side/end losses). With $L/D = 1.0$, the cylinder and disk explosive dimensions are identical. The particles were steel ($\rho = 7800$ kg/m^3) with a diameter of

25

$d_p = 5$ mm. To generate the initial locations of the closely packed particles, a mesh of triangular elements covering the surface of the explosive was generated with a cell size of 5 mm. Initial particle locations were then defined using the coordinates of the mesh vertices. The surface meshes were shrunk slightly to ensure that no particles were located on the symmetry planes. Table 3 gives the explosive radius $D/2$, explosive half length $L/2$, number of Lagrangian particles n_p, explosive mass m_c, and total particle mass $\sum m_p$ for the charge configurations as modeled (one-eighth of the full geometry).
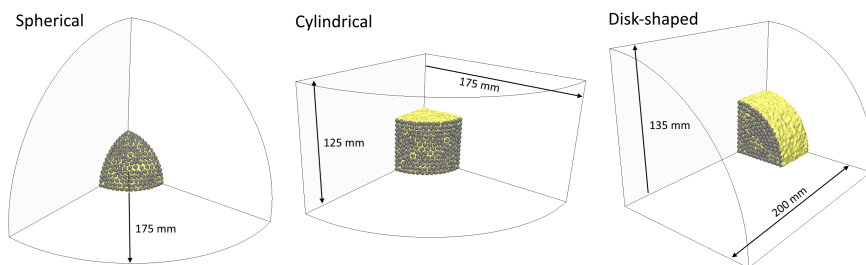

Figure 10: Simulation domains with dimensions for the sphere, cylinder, and disk charges with particles. Three symmetry planes are used in the 3D models.

Table 3: Explosive dimensions, explosive mass, number of particles, and total particle mass in the IED charge shape simulations.

Charge shape	$D/2$	$L/2$	m_c	n_p	$\sum m_p$
	(mm)	(mm)	(g)		(g)
Sph	50	-	105	167	85
Cyl ($L/D = 1.0$)	50	50	157	173	88
Cyl ($L/D = 1.2$)	50	60	188	205	105
Disk ($L/D = 1.0$)	50	50	157	83	42
Disk ($L/D = 0.833$)	60	50	226	125	64

A uniform cell size of $\delta = 2.5$ mm was used for the simulations. This gives 20 cells through the explosive thickness, and a particle diameter to cell size ratio of

26

$\delta/d_p = 0.5$. The explosives were center-initiated and the simulations were run to $t_{\text{sim}} = 80$ μs. Each simulation domain contained approximately 10^6 tetrahedral cells and required less than one hour to complete, running on 10 processors of the HP Z800 workstation. We define the variable

$$\Psi \equiv \frac{\mid \mathbf{x}_p^i(t_0) - \mathbf{x}_d \mid}{\min \mid \mathbf{x}_p^i(t_0) - \mathbf{x}_d \mid} \tag{33}$$

to express the initial particle position relative to the detonation point, $\mathbf{x}_d$. Particles at $\Psi = 1$ are nearest to the detonation point and expected to have the highest velocity. Figure 11 shows the particle terminal velocities plotted against Ψ. The multimaterial initialization on the unstructured grid gives a rough representation of the explosive surface, as shown in Figure 10. Because the particles are initially located on the explosive surface, interpolations between fluid and particles in the numerical model are subsequently affected. This causes a variation in V_T for particles at the same Ψ, as observed in the simulations. Limiting of the interphase coupling terms also contributes somewhat to the scatter in V_T. However, this limiting accounts for less than a 0.05% error in the total energy conservation for these simulations. Cubic polynomial curve fits to the terminal velocities, $\widetilde{V}_T(\Psi)$, are plotted. The average deviation relative to the fitted curves is ≤ 40 m/s for all cases. With the spherical charge, all particles are at $\Psi = 1$ as they are equidistant from the detonation point. As Ψ increases in the cylindrical and disk charges, the interaction between the detonation wave and particles transitions from a head-on to a side-on shock impact. Consequently, V_T rapidly decreases and particles on the edge of these charges have a smaller velocity component normal to the explosive surface.

Table 4 gives C/M ratios for the configurations, particle velocities from simulations, calculated Gurney velocities, and a ratio of simulated and Gurney velocities. Two Gurney velocities are given, the first assumes infinite length cylinders and infinite diameter disks ($V_{\text{G},\infty}$) and the second uses equations with side/end losses ($V_{\text{G,losses}}$). Gurney calculations assume a value of $\sqrt{2E} = 2.68$ km/s for C4. Note that C/M is increasing between the sphere, cylinder, and disk charges. The simulated fragment velocities are $\sim$40-55% of the $V_{\text{G},\infty}$ predic-
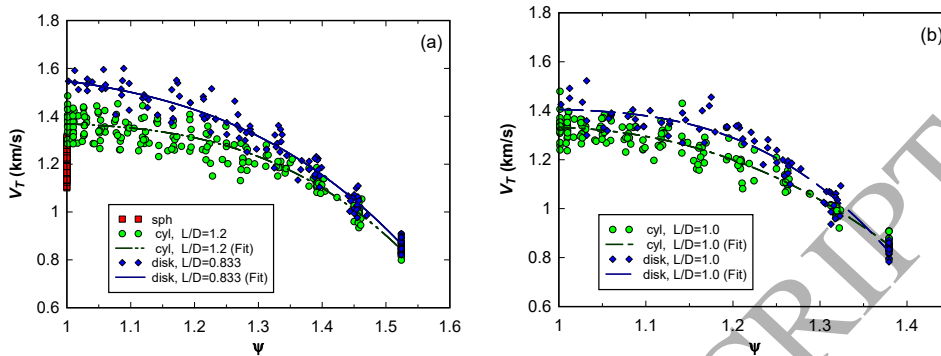
27

Figure 11: Final particle velocities versus relative initial positions, Ψ. Sphere, cylinder ($L/D = 1.2$), and disk ($L/D = 0.833$) charges are plotted in (a) and cylinder and disk with ($L/D = 1.0$) are in (b).

tions, implying that a large amount of energy is not transferred to the particles. Calculations with end losses show a somewhat better agreement, but the trend in fragment velocity versus configuration has reversed (i.e. the disk charges have to lowest $V_{\mathrm{G,losses}}$). The modified Gurney approach for finite charge sizes assumes a reduction in explosive energy due to explosive not in contact with metal [43]. However, this approach is not suited for the current configurations which have gaps between each particle. Nonetheless, simulations show that the side/end losses are important and there is a slight increase in $\widetilde{V}_T$ for the larger charges ($\sim 3\%$ increase for the $L/D = 1.2$ cylinder and $\sim 10\%$ increase for the $L/D = 0.833$ disk).

Previous work [6] has shown that the point-particle approach underestimates the velocity of explosive driven fragments. However, the current analysis provides relative comparison of V_T from various IED charge configurations. As a point of comparison, the experiments of Lixen et al. [44] with a conical/disk-shaped dense fragment generator produced fragment velocities ranging from 1.70 km/s at the center to 1.20 km/s in the periphery. These velocities are roughly 10-20% higher than those of the disk shaped IEDs in the current work, but had more confinement (i.e. a 5 mm casing around the charge and a 20 mm steel tamper).

28

Table 4: IED charge shape study results: charge to metal ratio, predicted fragment velocities from simulations and Gurney equations, and the ratio of predicted velocities.

Charge shape	C/M	$\widetilde{V}_T(\Psi = 1)$ (km/s)	$V_{G,\infty}$ (km/s)	$V_{G,\text{losses}}$ (km/s)	$\dfrac{\widetilde{V}_T(\Psi = 1)}{V_{G,\infty}}$
Sph	1.23	1.21	2.25	2.25	0.54
Cyl ($L/D = 1.0$)	1.78	1.33	2.60	2.12	0.51
Cyl ($L/D = 1.2$)	1.80	1.37	2.61	2.19	0.52
Disk ($L/D = 1.0$)	3.71	1.41	3.45	1.99	0.41
Disk ($L/D = 0.833$)	3.55	1.55	3.42	2.09	0.45

If we examine a particle at $\Psi = 1$ for each configuration, we observe that the particles accelerate rapidly after the shock passage, and nearly reach their terminal velocity after 30 μs. In each case, the unsteady forces ($\mathbf{F}_{\text{pg}}$ and $\mathbf{F}_{\text{am}}$) account for more than 90% of the total particle force. In the cylinder and disk configurations, the unsteady forces continue to act on the particle for a longer duration, contributing to higher velocities for those geometries.

3.4. IED blast on a bomb disposal technician

This numerical test case is inspired by the full-scale experiments on Explosive Ordinance Disposal (EOD) bomb suits described by Dionne et al. [45] and Bass et al. [31]. In the tests, a mannequin representing a 50th percentile North American male (height = 1.75 m, weight = 77 kg) was dressed in the EOD suit and placed in a kneeling positions to represent a common EOD work condition. The EOD mannequin was subjected to close range explosions from a 0.567 kg spherical C4 charge at chest height (77 cm) and approximately 60 cm standoff from the kneeling mannequin. The EOD suit is specifically designed to dissipate the blast and protect vital organs in the chest from compressive pressure loads and fragments.

We consider a scenario with a similar charge weight and standoff distance

29

from a kneeling anthropometric figure (the "bomb tech"). A schematic of the problem and computational domains are shown in Figure 12. The dimensions and shape of the bomb tech represent a 50th percentile male wearing an EOD suit with arms extended towards the IED. In the current models, the bomb tech

485 figure is modeled by rigid surfaces. This will allow us to assess risks from the primary blast and fragments, but not injuries related to the body acceleration (e.g. head and neck injury criteria). The explosive is a 0.5 kg cylinder of C4 ($L/D = 1.5$) which is surrounded by Lagrangian particles representing IED fragments. The particles are 6 mm steel spheres with an inter-particle spacing

490 of 2 mm. This gives 288 particles around the full charge with a total particle mass of 0.25 kg. The explosive is located in the middle of a bench that is 45 cm high, 40 cm wide, and 150 cm long. There is a solid wall behind the bench which reflects the blast wave. The center of the explosive is approximately 50 cm above the ground and 60 cm from the bomb tech. The simulation was

495 conducted in two steps. Step 1 has a domain size of 40×30×30 cm and includes the region surrounding the explosive, up to the edge of the bench. Step 2 has a larger domain size of 170×135×175 cm. Both domains assume symmetry along the $y = 0$ plane.

In step 1, the explosive is center-initiated and the simulation progresses until

500 the blast wave nearly reaches the domain boundary. Step 1 has a cell size of 2 mm near the explosive (giving 16 cells across the radius), then the cell size increases gradually to a maximum background cell size of 10 mm. The step 2 domain uses cell sizes of 8 mm over the initial explosive region, 12 mm near the bomb tech, and $\delta = 40$ mm for the background mesh. A summary of the mesh

505 and run times on the HP Z800 workstation is given in Table 5.

Simulation results at the end of step 1 ($t = 0.03$ ms) are shown in Figure 13. The blast wave forms a bell-shape, due to the cylindrical charge geometry and shock reflection off the bench surface. The particles have reached their maximum velocity of approximately 1100 m/s. The $z = 0$ isosurface denotes the interface

510 between the explosive detonation products and air.

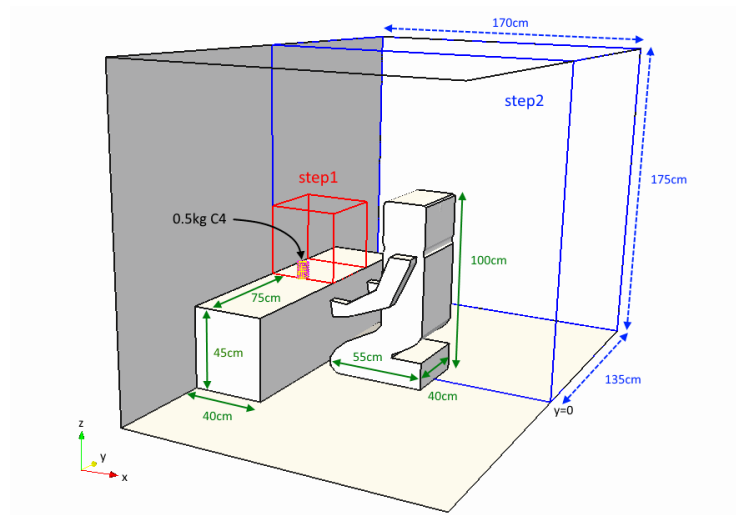In step 2, the blast wave and fragments propagate outward and impact the

30

Figure 12: Schematic of the EOD blast problem setup. Computational domains utilize a symmetry plane at $y = 0$.
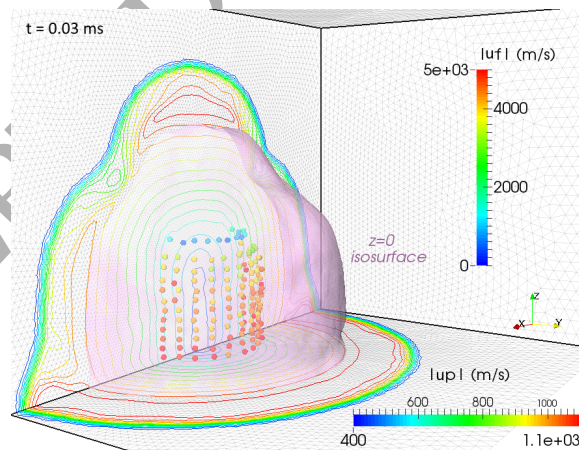

Figure 13: Velocity contours for the fluid ($|\mathbf{u}_\mathrm{f}|$) and particles ($|\mathbf{u}_\mathrm{p}|$) from step 1.

31

Table 5: Simulation details for the IED blast on an EOD bomb tech.

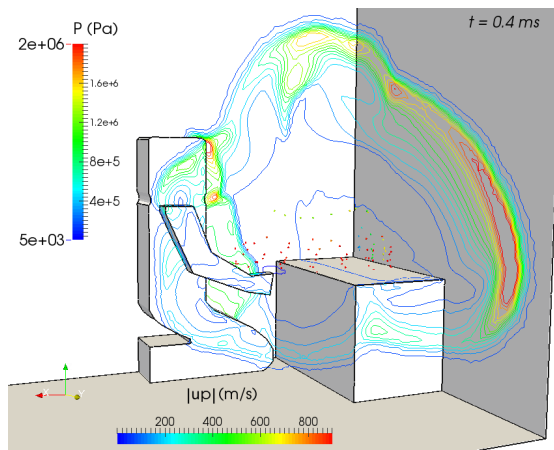| Step#	n_{el}	n_{CPU}	t_{sim} (ms)	t_{solve} (hr)
1	2.21×10^6	10	$0 - 0.03$	0.7
2	2.73×10^6	10	$0.03 - 4$	8.0

Figure 14: Contours of fluid pressure and particle velocities from step 2.

bomb tech. Blast pressures and fragment velocities at 0.4 ms after detonation are shown in Figure 14. There are Mach reflections along the bench surface and the back wall, resulting in high pressure shocks traveling outward along these surfaces. The shock wave impacts the front surface of the bomb tech at $t = 0.17$ ms, but the particles do not arrive until $t \approx 0.6$ ms. Figure 15 shows contours of maximum pressure and impulse on the domain surfaces of the completed simulation. Pressure and impulse around the explosive charge are very high, especially in the axial and radial directions due to the cylindrical charge shape. The high shock pressures attenuate rapidly with expansion, but shock reflections from the back wall and chest surface of the bomb tech cause localized high pressures in those regions. The shock is diffracted around the bomb tech and the blast impulse on the top (head), sides, and back are greatly
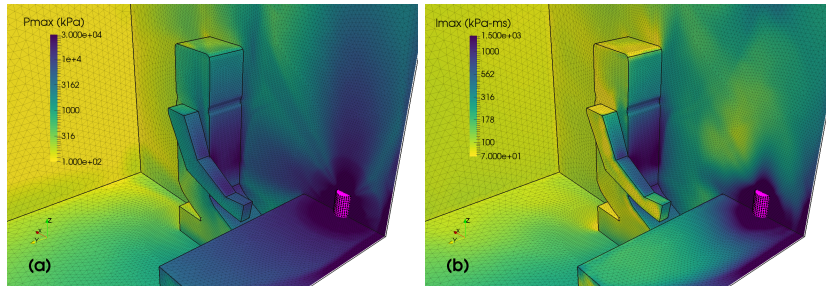
32

Figure 15: Maximum (a) pressure and (b) impulse tracked on the domain surfaces (contours plotted on a log scale). The IED is shown at the initial location.

reduced. Shocks reflected from the back wall and bench surfaces reach the bomb tech at ~1.0 ms after the initial shock, but do not significantly contribute to the impulse.

The models can be used to determine probable locations of fragment impacts, fragment velocity, and impulse. The protection levels of EOD suits are typically quantified by a "V50" ballistic rating, which expresses the velocity at which 50% of projectiles are stopped by the armor. These ratings are based on military standards, such as the STANAG 2920 which uses a 1.1 g fragment simulating projectile. The V50 ratings vary between suit manufacturers, designs, and the various suit components [46]. The 6 mm spherical fragments in the simulation have a mass of 0.88 g and velocities greater than 1000 m/s, which exceeds the V50 rating for many areas of the EOD suit. Therefore, it is possible that they could penetrate the EOD suit. However, critical areas of the suit, such as the chest, neck, and groin, can have additional reinforcement and a higher V50 rating (e.g. > 1500 m/s) and may be able to withstand IED fragments. This type of simulation can provide insight into specific EOD scenarios with IEDs, and can easily be modified for parameter studies of different IED types and environments.

33

4. Conclusions

This work has demonstrated the capabilities of a coupled Euler-Lagrange simulation method for assessing risk from IED threats in realistic scenarios. The increasing power of personal computers makes it possible to run larger and more detailed physics-based simulations which can play an important role in countering the growing threat of terrorism and IEDs.

The CFD solver has been validated using test data from an explosion in a partially confined cylinder. In this tunnel-like geometry, the blast quickly evolves into a one-dimensional type shock wave that is more powerful than an unconfined air blast. Two cases of explosions on a subway train platform have been simulated, with the predicted peak pressure and impulse were used to develop 3D visualizations of predicted injury probabilities in the domain. The enclosed geometry produces a complex blast wave profile with the impulse increasing over a period of tens of milliseconds. With the smaller 10 kg C4 charge, the extent of fatal lung injuries predicted by probit equations (based on the Bowen curves) are much lower than the Axelsson method. This highlights the need for more validation and improved human injury models which can be adopted in blast simulations. IED fragments have been modeled by coupling the CFD solver with a Lagrangian point-particle approach. Geometry of the IED directly influences the acceleration and terminal velocities of fragments surrounding the charge. Particles around cylindrical and disk charges (both with $L/D = 1.0$) have terminal velocities that are 10% and 16% higher, respectively, than a spherical charge with the same effective charge thickness (albeit different C/M ratios). Fragment velocities predicted by Gurney equations without end losses were higher than the simulations by roughly 40-55%. This implies that a large amount of detonation energy is not transferred to the metal due to gaps between the particles. Numerical simulation of an IED blast on a bomb disposal technician shows the ability to assess risks from shock and fragment loading in the near field. While EOD suits are designed to withstand close range detonation, IEDs produce high speed fragments which may exceed the

34

suits' ballistic rating.

Developing better predictive tools for real-life IED scenarios is valuable for the future of emergency response planning. Future work will investigate increas-
₅₇₅ ing robustness of the particle method, for larger particles and smaller charges, and extending the blast risk evaluation models for scenarios of crowded areas.

References

[1] J. L. Arnold, P. Halpern, M.-C. Tsai, H. Smithline, Mass casualty terrorist bombings: A comparison of outcomes by bombing type, Ann. Emerg. Med.
₅₈₀   43 (2004) 263 – 273.

[2] H. R. Champion, J. B. Holcomb, L. A. Young, Injuries from explosions: physics, biophysics, pathology, and required research focus, J. Trauma 66 (2009) 1468–77.

[3] R. Golan, D. Soffer, A. Givon, K. Peleg, The ins and outs of terrorist
₅₈₅   bus explosions: Injury profiles of on-board explosions versus explosions occurring adjacent to a bus, Injury 45 (2014) 39 – 43.

[4] N. Elsayed, J. Atkins, Explosion and Blast-Related Injuries: Effects of Explosion and Blast from Military Operations and Acts of Terrorism, Elsevier Science, 2010.

₅₉₀ [5] M. A. Price, V.-T. Nguyen, O. Hassan, K. Morgan, A method for compressible multimaterial flows with condensed phase explosive detonation and airblast on unstructured grids, Comput. Fluids 111 (2015) 76–90.

[6] M. A. Price, V.-T. Nguyen, O. Hassan, K. Morgan, An Euler-Lagrange particle approach for modeling fragments accelerated by explosive detonation,
₅₉₅   Int. J. Numer. Methods Eng. 106 (2016) 904–926.

[7] T. Rose, P. Smith, Influence of the principal geometrical parameters of straight city streets on positive and negative phase blast wave impulses, Int. J. Impact Eng. 27 (2002) 359 – 376.

35

[8] R. Löhner, F. F. Camelli, J. D. Baum, Large-scale blast calculations on massively parallel machines, in: 22nd Int. Symp. Mil. Aspects of Blast and Shock, Bourges, France, 2012.

[9] D. L. Rice, J. D. Baum, F. Togashi, R. Löhner, A. Amini, First-principles blast diffraction simulations on a notebook: accuracy, resolution and turn-around issues, in: 20th Int. Symp. Mil. Aspects of Blast and Shock, Oslo, Norway, 2008.

[10] W. Baker, Explosion Hazards and Evaluation, Fundamental studies in engineering, Elsevier Scientific Publishing Company, 1983.

[11] O. Pennetier, M. William-Louis, A. Langlet, Numerical and reduced-scale experimental investigation of blast wave shape in underground transportation infrastructure, Process Saf. Environ. 94 (2015) 96 – 104.

[12] G. Giannopoulos, M. Larcher, F. Casadei, G. Solomos, Risk assessment of the fatality due to explosion in land mass transport infrastructure by fast transient dynamic analysis, J. Hazard. Mater. 173 (2010) 401 – 408.

[13] M. Larcher, F. Casadei, G. Solomos, Risk analysis of explosions in trains by fluid–structure calculations, J. Transp. Secur. 3 (2010) 57–71.

[14] O. Soto, J. Baum, R. Löhner, An efficient fluid-solid coupled finite element scheme for weapon fragmentation simulations, Eng. Fract. Mech. 77 (2010) 549 – 564.

[15] Y. Ling, A. Haselbacher, S. Balachandar, Importance of unsteady contributions to force and heating for particles in compressible flows: Part 1: Modeling and analysis for shock–particle interaction, Int. J. Multiphase Flow 37 (2011) 1026 – 1044.

[16] K. Balakrishnan, D. Nance, S. Menon, Simulation of impulse effects from explosive charges containing metal particles, Shock Waves 20 (2010) 217–239.

36

[17] V.-T. Nguyen, H. H. Nguyen, M. A. Price, J. K. Tan, Shock capturing schemes with local mesh adaptation for high speed compressible flows on three dimensional unstructured grids, Comput. Fluids 70 (2012) 126 – 135.

[18] G. Allaire, S. Clerc, S. Kokh, A five-equation model for the simulation of interfaces between compressible fluids, J. Comput. Phys. 181 (2002) 577 – 616.

[19] R. Saurel, R. Abgrall, A multiphase Godunov method for compressible multifluid and multiphase flows, J. Comput. Phys. 150 (1999) 425 – 467.

[20] K.-M. Shyue, A fluid-mixture type algorithm for compressible multicomponent flow with Mie-Grüneisen equation of state, J. Comput. Phys. 171 (2001) 678 – 707.

[21] B. Dobratz, P. Crawford, LLNL Explosives Handbook: Properties of Chemical Explosives and Explosive Simulants, UCRL-52997, Lawrence Livermore National Laboratory, 1985.

[22] R. C. Ripley, F. Zhang, F.-S. Lien, Acceleration and heating of metal particles in condensed matter detonation, Proc. R. Soc. Lond. A 468 (2012) 1564–1590.

[23] E. Loth, Compressibility and rarefaction effects on drag of a spherical particle, AIAA Journal 46 (2008) 2219–2228.

[24] M. Parmar, A. Haselbacher, S. Balachandar, On the unsteady inviscid force on cylinders and spheres in subcritical compressible flow, Proc. R. Soc. Lond. A 366 (2008) 2161–2175.

[25] N. P. Weatherill, O. Hassan, Efficient three-dimensional Delaunay triangulation with automatic point creation and imposed boundary constraints, Int. J. Numer. Methods Eng. 37 (1994) 2005–2039.

[26] E. Toro, M. Spruce, W. Speares, Restoration of the contact surface in the HLL-Riemann solver, Shock Waves 4 (1994) 25–34.

37

[27] T. Barth, D. Jespersen, The design and application of upwind schemes on unstructured meshes, AIAA paper (1989) 89–0366.

655 [28] A. Jameson, W. Schmidt, E. Turkel, Numerical solution of the Euler equations by finite volume methods using Runge-Kutta time-stepping schemes, in: AIAA Paper, 1981.

[29] M. W. Courtney, A. C. Courtney, Working toward exposure thresholds for blast-induced traumatic brain injury: Thoracic and acceleration mech-
660 anisms, NeuroImage 54, Suppl. 1 (2011) S55 – S61.

[30] F. Lees, Loss Prevention in the Process Industries (2nd Edition), Elsevier Scientific Publishing Company, 1996.

[31] C. D. Bass, M. Davis, K. Rafaels, M. S. Rountree, R. M. Harris, E. Sanderson, W. Andrefsky, G. DiMarco, M. Zielinski, A methodology for assessing
665 blast protection in explosive ordnance disposal bomb suits, Int. J. Occup. Saf. Ergon. 11 (2005) 347–361.

[32] J. G. Bowen, E. R. Fletcher, D. R. Richmond, Estimate of Mans Tolerance to the Direct Effects of Air Blast, Lovelace Foundation for Medical Education and Research, Albuquerque, NM, 1968.

670 [33] Committee for the Prevention of Disasters, Methods for the determination of possible damage to people and objects resulting from releases of hazardous materials, [1st ed.] ed., Voorburg : Director-General of Labour, 1992.

[34] J. Teland, J. van Doormaal, Blast wave injury prediction models for complex scenarios, in: 22nd Int. Symp. Mil. Aspects of Blast and Shock,
675 Bourges, France, 2012.

[35] C. R. Bass, K. A. Rafaels, R. S. Salzar, Pulmonary injury risk assessment for short-duration blasts, J. Trauma Acute Care Surg. 65 (2008) 604–615.

[36] H. Axelsson, J. T. Yelverton, Chest wall velocity as a predictor of nonaudiory blast injury in a complex wave environment, J. Trauma 40 (1996) S31–7.

[37] J. van Doormaal, M. van der Horst, An approximation procedure of the axelsson model for quick injury prediction, in: 21st Int. Symp. Mil. Aspects of Blast and Shock, Jerusalem, Israel, 2010.

[38] F. Díaz-Alonso, E. G. Ferradás, J. F. S. Pérez, A. M. Aznar, J. R. Gimeno, J. M. Alonso, Consequence analysis by means of characteristic curves to determine the damage to humans from the detonation of explosive substances as a function of TNT equivalence, J. Loss Prev. Proc. 20 (2007) 187 – 193.

[39] R. C. Ripley, F. Zhang, C. T. Cloney, S. McClennan, N. McCormick, A modern blast solver strategy and its urban application, in: 23rd Int. Symp. Mil. Aspects of Blast and Shock, Oxford, UK, 2014.

[40] B. Zakrisson, B. Wikman, H.-Å. Häggblad, Numerical simulations of blast loads and structural deformation from near-field explosions in air, Int. J. Impact Eng. 38 (2011) 597 – 612.

[41] M. A. Price, V.-T. Nguyen, H. H. Nguyen, J. K. Tan, C. Chew, T. Karasek, Computational framework for simulation of air blast and structural interactions, in: 22nd Int. Symp. Mil. Aspects of Blast and Shock, Bourges, France, 2012.

[42] W. E. Baker, J. J. Kulesz, P. S. Westine, P. A. Cox, J. S. Wilbeck, Manual for the Prediction of Blast and Fragment Loadings on Structures (DOE/TIC-11268), 1992.

[43] D. Crabtree, S. Waggener, Gurney-type formulas for estimating initial fragment velocities for various warhead geometries, Naval Surface Weapons Center, Dahlgren, VA, NSWC TR 86–241 (1987) 1–44.

39

[44] Q. Lixin, Q. Ming, W. Yu, Z. Yongqing, J. Daojian, Dense fragment generator, Propell. Explos. Pyrot. 27 (2002) 267–278.

[45] J. Dionne, J. Nerenberg, A. Makris, Reduction of blast-induced concussive injury potential and correlation with predicted blast impulse, in: 17th Int. Symp. Mil. Aspects of Blast and Shock, Las Vegas, USA, 2002.

[46] G. Winfield, Bomb suit roundup, CBRNe World Summer (2009) 100.